Low-energy theory for the graphene twist bilayer

D. Weckbecker,[1,*] S. Shallcross,[1,†] M. Fleischmann,[1] N. Ray,[1] S. Sharma,[2,3] and O. Pankratov[1]

[1]*Lehrstuhl für Theoretische Festkörperphysik, Staudtstrasse 7-B2, 91058 Erlangen, Germany*

[2]*Max-Planck-Institut für Mikrostrukturphysik, Weinberg 2, 06120 Halle, Germany*

[3]*Department of Physics, Indian Institute of Technology, Roorkee, 247667 Uttarkhand, India*

(Received 8 September 2015; published 27 January 2016)

The graphene twist bilayer represents the prototypical system for investigating the stacking degree of freedom in few-layer graphenes. The electronic structure of this system changes qualitatively as a function of angle, from a large-angle limit in which the two layers are essentially decoupled—with the exception of a 28-atom commensuration unit cell for which the layers are coupled on an energy scale of ≈8 meV—to a small-angle strong-coupling limit. Despite sustained investigation, a fully satisfactory theory of the twist bilayer remains elusive. The outstanding problems are (i) to find a theoretically unified description of the large- and small-angle limits, and (ii) to demonstrate agreement between the low-energy effective Hamiltonian and, for instance, *ab initio* or tight-binding calculations. In this article, we develop a low-energy theory that in the large-angle limit reproduces the symmetry-derived Hamiltonians of Mele [Phys. Rev. B **81**, 161405 (2010)], and in the small-angle limit shows almost perfect agreement with tight-binding calculations. The small-angle effective Hamiltonian is that of Bistritzer and MacDonald [Proc. Natl. Acad. Sci. (U.S.A.) **108**, 12233 (2011)], but with the momentum scale ΔK, the difference of the momenta of the unrotated and rotated special points, replaced by a *coupling momentum scale* $g^{(c)} = \frac{8\pi}{\sqrt{3}a} \sin\frac{\theta}{2}$. Using this small-angle Hamiltonian, we are able to determine the complete behavior as a function of angle, finding a complex small-angle clustering of van Hove singularities in the density of states (DOS) that after a "zero-mode" peak regime between $0.90^\circ < \theta < 0.15^\circ$ limits $\theta < 0.05^\circ$ to a DOS that is essentially that of a superposition DOS of all bilayer stacking possibilities. In this regime, the Dirac spectrum is entirely destroyed by hybridization for $-0.25 < E < 0.25$ eV with an average band velocity $\approx 0.3 v_F^{(\mathrm{SLG})}$ (where SLG denotes single-layer graphene). We study the fermiology of the twist bilayer in this limit, finding remarkably structured constant energy surfaces with multiple Lifshitz transitions between K- and Γ-centered Fermi sheets and a rich pseudospin texture.

DOI: 10.1103/PhysRevB.93.035452

I. INTRODUCTION

The rich physics associated with the interlayer degree of freedom in few-layer graphenes is manifest perhaps most strikingly in the graphene twist bilayer system. This system, consisting of two mutually rotated layers of graphene, exhibits a wide range of electronic effects as a function of the twist angle, and it has attracted sustained attention from both theory and experiment [1–24]. The electronic structure of the twist bilayer is both diverse at the single-particle level and challenging to the naive application of band theory. The failure of a straightforward band theory approach lies in the fact that the twist angle of the bilayer, which obviously fixes all physical properties, is insufficient to define the lattice vectors of the system. The classical picture of backfolded bands in a twist bilayer Brillouin zone hybridizing to open a gap leading to van Hove singularities in the density of states evidently cannot hold: there is no unique bilayer Brillouin zone. In fact, it has been shown that the system is endowed with an emergent coupling momentum scale that depends only on the twist angle of the bilayer. Real-space periodicity is thus a physically irrelevant property of the twist bilayer for the electronic structure [5]. The electronic structure itself is enormously rich and can be characterized by three regimes: a large-angle regime in which the two layers are essentially decoupled, an intermediate-angle regime in which van Hove singularities move toward the Dirac point renormalizing the Fermi velocity, and a small-angle regime in which van Hove singularities are dense in energy near the Dirac point, and the two layers are strongly coupled. In real space, this small-angle regime is associated with the emergence of a geometric moiré lattice, and electron localization on the "AA spots" of this moiré.

The large-angle regime has been studied *ab initio* with the finding that the Dirac point degeneracy generally found at large angles is, for the smallest 28-atom unit cell commensuration, lifted on an energy scale of ≈8 meV [18–21]. Within this window, the band structure shows either a sublattice exchange (SE) even (C_3) or a Bernal bilayer (C_6) form depending on the point-group symmetry of the bilayer, in agreement with a large-angle continuum theory of the twist bilayer [15]. The recent work of Kazuyuki *et al.* has taken the *ab initio* approach to the beginning of the strongly coupled regime [25], where they find the first "magic angle" at which the Fermi velocity vanishes to be 1.1°. However, as the minimum number of atoms to realize a supercell is $N = 1/2 \sin^2\theta$ with $\theta = \cos^{-1}(3q^2 - 1)/(3q^2 + 1)$, $q \in \mathbb{N}$, q odd, the *ab initio* approach cannot, with the present state of the art, penetrate the small-angle regime. Semiempirical tight-binding calculations have been used to explore the small-angle regime [13,16,26] finding a complex clustering of moiré bands at the Dirac point. Finite flakes of the graphene twist bilayer have also been calculated in the tight-binding scheme, where it has been shown that, remarkably, a single moiré unit cell in a finite geometry is sufficient to reproduce the density of states and electron density of the

*Dominik.Weckbecker@fau.de

†sam.shallcross@fau.de

extended twist bilayer [2]. For rotation angles smaller than about 0.8°, however, even the tight-binding approach reaches computational limits. To explore the physics below this angle a tight-binding scheme with a single-layer graphene (SLG) basis set [5] and effective Hamiltonians obtained from various expansions of the tight-binding method [8,22,27–29] have been developed. Of these effective Hamiltonian approaches, perhaps the most elegant is that due to Bistritzer *et al.* [8], which consists of two Dirac-Weyl operators coupled by a real-space moiré field $S(\mathbf{r})$, which possesses the peculiar feature of having a periodicity exactly $\sqrt{3}$ larger than the moiré length $D = \frac{1}{2\sin\theta/2}$ (we present all real-space quantities in units of the SLG lattice constant a, and reciprocal space quantities in units of $2\pi/a$). Calculations based on this Hamiltonian revealed a series of angles at which the band velocity at the Dirac point vanished, the so called magic angles. The SLG basis approach of Shallcross *et al.* revealed both the existence of the coupling momentum scale $g^{(c)} = \frac{4}{\sqrt{3}}\sin\frac{\theta}{2}$ as well as the emergence of an approximately self-similar peak in the density of states at the smallest angles that could be reached (0.46°).

While the state of understanding of a twist bilayer band structure would appear to be impressively complete, a number of questions remain. First, the low-energy Dirac-like Hamiltonian of Bistritzer *et al.* [8] has been reported to require rescaling [26] in order to reproduce band structures and velocity renormalization found from tight-binding calculations, throwing into doubt the validity of the low-energy approach. Furthermore, the continuum theories presented in the literature do not clearly relate the origin of the low-energy physics of twisted bilayer graphene to the crucial role the momentum scale $g^{(c)}$ plays in the interlayer coupling. It also remains unclear what connection there is, if any, between the small-angle [8,22] and large-angle continuum models [29]. These questions are not merely academic: the twist bilayer continues to be intensely investigated, with more recent work looking at many-body effects [30–33] or more complex manifestations of the twist geometry [34]. It is important, therefore, to clarify the "fruit fly" model of twist stacking physics: the single-particle physics of the twist bilayer.

To clarify this situation, in this paper we derive a low-energy continuum Hamiltonian for twisted bilayer graphene, making direct use of the $g^{(c)}$ coupling momentum scale, and we show that it agrees perfectly with tight-binding calculations in the intermediate and small-angle limit. The form of this low-energy Hamiltonian is identical to that derived by Bistritzer *et al.*, but with the momentum scale $\Delta K = \frac{4}{3}\sin\frac{\theta}{2}$ replaced by $g^{(c)}$. Interestingly, the resulting moiré field $S(\mathbf{r})$ now has exactly the periodicity of the real-space moiré lattice. The numerical efficiency of the low-energy approach allows us to completely characterize constant energy surfaces, band velocities, and density of states in the small-angle limit for $0.03° < \theta < 1.2°$.

Furthermore, we derive from the tight-binding method a large-angle continuum model in which the interlayer interaction is expressed as a multiple scattering series through high-energy states. This reproduces the large-angle symmetry-derived continuum Hamiltonians [15], but with all parameters fixed by the underlying electronic theory, and again it shows near perfect agreement with full tight-binding calculations. The small- and large-angle limits are thus conceptually unified by the notion of multiple scattering through high-energy states, with the principal difference between the large- and small-angle limits being simply a vast increase in the number of scattering paths required in the small-angle limit, which is encoded in a real-space moiré field $S(\mathbf{r})$.

The remainder of this article is structured as follows. In Sec. II we rederive the momentum scale $g^{(c)}$ as a selection rule for the coupling of single-layer Bloch states, and in the subsequent two sections we develop fully electronic low-energy continuum approximations based on this selection rule for both the large- (Sec. III) and small- (Sec. IV) angle regimes. We then explore in detail the single-particle properties in the small-angle regime: in Sec. VI we calculate the density of states and electron density in the very small-angle limit, finding remarkable accuracy between the continuum and tight-binding approaches, and in Sec. VII we consider how the band velocity behaves as a function of twist angle and energy (of which the magic angles represent a special $E = 0$ case), and we also describe the rich Fermi surface topology as a function of both rotation angle as well as doping. Thereafter, we summarize our results and discuss possible future research in Sec. VIII.

II. SELECTION RULE FOR SINGLE-LAYER BLOCH STATES

In this section, we will recast the two-center tight-binding method in a way that will subsequently provide a transparent route to a low-energy description of the twist bilayer, for both large and small twist angles. These two limits will be conceptually unified by possessing the same fundamental *form* for the way in which Bloch functions (or single-layer eigenstates) from each layer are coupled by the interaction. We consider the Bloch functions

$$\left|\phi^{(n)}_{\alpha\mathbf{k}_n}\right\rangle = \frac{1}{\sqrt{N}}\sum_{\mathbf{R}_n} e^{i\mathbf{k}_n\cdot(\mathbf{R}_n+\boldsymbol{\nu}^{(n)}_\alpha)}\left|\mathbf{R}_n+\boldsymbol{\nu}^{(n)}_\alpha\right\rangle, \tag{1}$$

where $\mathbf{R}_n$ runs over all lattice sites in the nth layer, $\boldsymbol{\nu}^{(n)}_\alpha$ represents the layer n basis vectors, and $1/\sqrt{N}$ denotes a normalization factor. We will first consider interlayer matrix elements in this basis. These are given by

$$\left\langle\phi^{(1)}_{\alpha\mathbf{k}_1}\middle|H\middle|\phi^{(2)}_{\beta\mathbf{k}_2}\right\rangle = \frac{1}{N}\sum_{\mathbf{R}_1\mathbf{R}_2} e^{-i\mathbf{k}_1\cdot(\mathbf{R}_1+\boldsymbol{\nu}^{(1)}_\alpha)}e^{i\mathbf{k}_2\cdot(\mathbf{R}_2+\boldsymbol{\nu}^{(2)}_\beta)} \times \underbrace{\left\langle\mathbf{R}_1+\boldsymbol{\nu}^{(1)}_\alpha\middle|H\middle|\mathbf{R}_2+\boldsymbol{\nu}^{(2)}_\beta\right\rangle}_{t(|\mathbf{R}_2+\boldsymbol{\nu}^{(2)}_\beta-\mathbf{R}_1-\boldsymbol{\nu}^{(1)}_\alpha|)}. \tag{2}$$

Writing the hopping function t in this expression in terms of its Fourier transform $t(r) = 1/(2\pi)^2\int d\mathbf{q}\, e^{-i\mathbf{r}\cdot\mathbf{q}}t(q)$ and performing the resulting phase sums with the help of the Poisson sum formula, we find a reciprocal space representation of this matrix element given by

$$\left\langle\phi^{(1)}_{\alpha\mathbf{k}_1}\middle|H\middle|\phi^{(2)}_{\beta\mathbf{k}_2}\right\rangle = \frac{\Omega}{(2\pi)^2}\sum_i t(\mathbf{k}_1+\tilde{\mathbf{G}}_{1i})[M_i]_{\alpha\beta} \tag{3}$$

with Ω the area of the single-layer graphene Brillouin zone and where the M_i matrices are defined as

$$[M_i]_{\alpha\beta} = e^{i\tilde{\mathbf{G}}_{1i}\cdot\boldsymbol{\nu}^{(1)}_\alpha}e^{-i\mathbf{R}\tilde{\mathbf{G}}_{2i}\cdot\boldsymbol{\nu}^{(2)}_\beta}, \tag{4}$$

with $\tilde{\mathbf{G}}_{1i}$ and $\mathbf{R}\tilde{\mathbf{G}}_{2i}$ representing the ith solution to the interlayer momentum-conservation equation

$$\mathbf{G}_1 = \mathbf{R}\mathbf{G}_2 + \mathbf{k}_2 - \mathbf{k}_1, \tag{5}$$

and where $\mathbf{G}_1$ and $\mathbf{R}\mathbf{G}_2$ represent reciprocal-lattice vectors in layers 1 and 2, respectively. It is this equation, and not those that describe the lattice commensuration, that determines the interlayer coupling. To see this, we note that if the momentum of the Bloch state $\mathbf{k}_1$ lies at the high-symmetry K point $\mathbf{K}_1 = (2/3,0)$ of the graphene Brillouin zone, then if the second-layer Bloch state has momenta $\mathbf{k}_2 = \mathbf{k}_1$, we can set $\mathbf{G}_1 = \mathbf{R}\mathbf{G}_2 = \mathbf{0}$ to solve Eq. (5) and yield a coupling constant of $\approx t(|\mathbf{K}_1|) = t(K)$ in the matrix element sum Eq. (3). For $\mathbf{k}_2 - \mathbf{k}_1 = \mathbf{G}_i^{(c)} - \mathbf{R}\mathbf{G}_i^{(c)}$, with $\mathbf{G}_i^{(c)}$ a reciprocal vector connecting $\mathbf{K}_1$ to one of the other two equivalent K points $\mathbf{K}_2$ and $\mathbf{K}_3$ of the Brillouin zone, i.e., $\mathbf{K}_2 = \mathbf{K}_1 + \mathbf{G}_2^{(c)}$ and $\mathbf{K}_3 = \mathbf{K}_1 + \mathbf{G}_3^{(c)}$, we will also evidently find a coupling constant of $\approx t(K)$. All other reciprocal vectors $\mathbf{G}$ will yield a momentum $\mathbf{K}_1 + \mathbf{G}$ that is outside the first Brillouin zone and hence a much reduced coupling constant $t(\mathbf{K}_1 + \mathbf{G}) \ll t(K)$. Thus only layer 1 and layer 2 Bloch states that have momenta satisfying

$$\begin{aligned}\mathbf{k}_2 - \mathbf{k}_1 &= \mathbf{G}_i^{(c)} - \mathbf{R}\mathbf{G}_i^{(c)} \\ &= \mathbf{g}_i^{(c)}\end{aligned} \tag{6}$$

will yield a significant order $\approx t(K)$ contribution to the matrix element sum and hence a non-negligible matrix element $\langle \phi^{(1)}_{\alpha\mathbf{k}_1} | H | \phi^{(2)}_{\beta\mathbf{k}_2} \rangle$. The vectors $\mathbf{g}_i^{(c)}$ may easily be calculated from Eq. (6) yielding

$$\mathbf{g}_1^{(c)} = \mathbf{0}, \tag{7}$$

$$\mathbf{g}_2^{(c)} = g^{(c)} \begin{pmatrix} \cos(\pi/3 + \theta/2) \\ \sin(\pi/3 + \theta/2) \end{pmatrix}, \tag{8}$$

$$\mathbf{g}_3^{(c)} = -g^{(c)} \begin{pmatrix} \cos(\pi/3 - \theta/2) \\ -\sin(\pi/3 - \theta/2) \end{pmatrix}, \tag{9}$$

where the *length scale* of the coupling in momentum space is given by $g^{(c)} = 4/\sqrt{3}\sin\frac{\theta}{2}$. In contrast to the momentum scale provided by the reciprocal-lattice vectors of the twist bilayer, which cannot be fixed by the rotation angle, Eqs. (7)–(9) depend *only on the twist angle of the bilayer*. This is exactly the momentum scale derived in Ref. [5] on symmetry grounds, and it represents the fundamental momentum scale on which Bloch functions (or single-layer basis functions derived from them) interact through the interlayer interaction. The M_i matrices in Eq. (3) take on a particularly simple form for the $G_i^{(c)}$, and they are given in Table I for the three principal stacking types of AA, AB, and AC stacking. It should be noted that Eqs. (7)–(9) are valid only near the high-symmetry K point given by $\mathbf{K} = (2/3,0)$; at other high-symmetry K points, Eqs. (7)–(9) are replaced by $\mathbf{g}_i^{(c)} = U\mathbf{g}_i^{(c)}$ with U the point-group operation that relates the two high-symmetry K points.

The intralayer matrix elements have a much simpler structure due to the fact that the equivalent of the interlayer momentum conservation, Eq. (5), is simply $\mathbf{k}_1 = \mathbf{k}_2$. Such matrix elements are thus given by

$$\langle \phi^{(n)}_{\alpha\mathbf{k}_1} | H | \phi^{(n)}_{\beta\mathbf{k}_2} \rangle = \delta_{\mathbf{k}_1\mathbf{k}_2} \frac{\Omega}{(2\pi)^2} \sum_i t(\mathbf{k}_1 + \mathbf{G}_{1i})[M_i]_{\alpha\beta}, \tag{10}$$

where the sum is now over all first-layer reciprocal-lattice vectors $\mathbf{G}_1$. As before, for Bloch state momenta $\mathbf{k}_1$ close to a high-symmetry K point it will be sufficient to employ the "first star" approximation and include only those $\mathbf{G}_1$ that yield $t(\mathbf{k}_1 + \mathbf{G}_1) \approx t(K)$. The M_i matrices are then given by the SLG entry of Table I.

TABLE I. The matrices M_i that appear in the formula for the interlayer interaction, Eq. (3), in the absence of umklapp scattering processes. Shown are the resulting matrices for three different types of initial stacking of the bilayer prior to rotation; AA, AB, and AC stacking.

Stacking type	$\mathbf{G}_1^{(c)} = (0,0)$	$\mathbf{G}_2^{(c)} = (-1, +\frac{1}{\sqrt{3}})$	$\mathbf{G}_3^{(c)} = (-1, -\frac{1}{\sqrt{3}})$
AA/SLG	$\begin{pmatrix} 1 & 1 \\ 1 & 1 \end{pmatrix}$	$\begin{pmatrix} 1 & e^{-i2\pi/3} \\ e^{+i2\pi/3} & 1 \end{pmatrix}$	$\begin{pmatrix} 1 & e^{+i2\pi/3} \\ e^{-i2\pi/3} & 1 \end{pmatrix}$
AB	$\begin{pmatrix} 1 & 1 \\ 1 & 1 \end{pmatrix}$	$\begin{pmatrix} 1 & e^{+i2\pi/3} \\ e^{+i2\pi/3} & e^{-i2\pi/3} \end{pmatrix}$	$\begin{pmatrix} 1 & e^{-i2\pi/3} \\ e^{-i2\pi/3} & e^{+i2\pi/3} \end{pmatrix}$
AC	$\begin{pmatrix} 1 & 1 \\ 1 & 1 \end{pmatrix}$	$\begin{pmatrix} e^{-i2\pi/3} & e^{+i2\pi/3} \\ e^{+i2\pi/3} & 1 \end{pmatrix}$	$\begin{pmatrix} e^{+i2\pi/3} & e^{-i2\pi/3} \\ e^{-i2\pi/3} & 1 \end{pmatrix}$

III. LOW-ENERGY THEORY AT LARGE TWIST ANGLES

As a first application of the Bloch state selection rule described in the previous section, we consider the electronic spectrum of twist bilayer systems with large rotation angles. As is by now well established, the spectrum of a large-angle twist bilayer ($15^\circ < \theta < 45^\circ$) is essentially that of two degenerate single-layer graphene spectra. This degeneracy is, however, broken at the Dirac point such that for the smallest commensuration unit cells of 28-carbon atoms (corresponding to rotation angles of $\theta = 21.79^\circ$ and 38.21°), the splitting at the Dirac point is of the order of 8 meV. The magnitude of this splitting decreases very rapidly with increasing supercell size, and it is only for the 28-atom unit cells that it can be considered a potentially measurable effect. The band structure near the Dirac point is also interesting as one finds a SE even structure for the case in which the twist bilayer possesses C_3 symmetry, while an AB bilayer type band structure is found for the higher-symmetry C_6 case. In this section, we will develop a general low-energy theory for the large-angle regime. This will yield low-energy effective Hamiltonians that agree with the form presented by Mele in Ref. [15], where they were derived on general symmetry grounds, but with all parameters of the theory clearly derived from the underlying tight-binding formalism.

A complete basis for the solution of the twist bilayer electronic structure at $\mathbf{k}_0$ [a $\mathbf{k}$ vector in the twist bilayer first Brillouin zone (BZ)] is given by the union of the set of first-layer Bloch functions with momenta $\mathbf{k}_1 = \mathbf{k}_0 + i_1\mathbf{g}_1^{(c)} + i_2\mathbf{g}_2^{(c)}$ that fall within the first BZ of the unrotated reciprocal space lattice, and the set of second-layer Bloch functions with momenta $\mathbf{k}_2 = \mathbf{k}_0 + i_1\mathbf{g}_1^{(c)} + i_2\mathbf{g}_2^{(c)}$ that fall within the

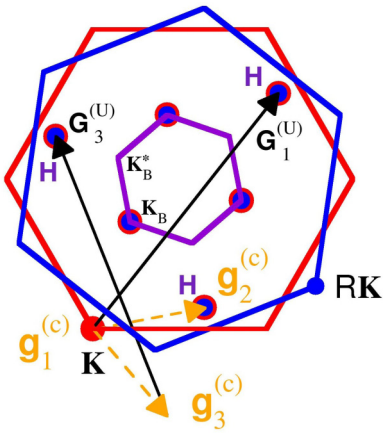

FIG. 1. Backfolding of single-layer graphene states to the bilayer Brillouin zone, where the **k** vector in the bilayer Brillouin zone to which basis states fold back has been set to $\mathbf{K}_B$. Also shown are the high-energy states that couple to **K** by the coupling momenta $\mathbf{g}_i^{(c)}$. For two of these ($\mathbf{g}_1^{(c)}$ and $\mathbf{g}_3^{(c)}$), these high-energy states lie outside the second-layer (rotated) Brillouin zone, and umklapp vectors are required to backfold them. The three high-energy **k** vectors involved in the scattering paths used in constructing the large-angle continuum Hamiltonians are labeled as "H."

second-layer BZ. Each **k** vector contributes two Bloch functions to the basis due to the two-atom primitive cell. An illustration of the **k** vectors contributing to the basis may be seen in Fig. 1. In this basis, we write the tight-binding Hamiltonian as

$$H = \begin{pmatrix} H_L & V_c \\ V_c^\dagger & H_H \end{pmatrix}, \tag{11}$$

where a matrix element $[H]_{\alpha\mathbf{k}_1 n,\beta\mathbf{k}_2 m} = \langle\phi^{(n)}_{\alpha\mathbf{k}_1}|H|\phi^{(m)}_{\beta\mathbf{k}_2}\rangle$. We organize the Hamiltonian such that H_L consists of the basis elements arising from the low-energy basis functions close to the K points of each layer (these are **K** and **RK** in Fig. 1); there will be two such basis functions from each layer and thus H_L is a 4×4 matrix. The H_H block consists of matrix elements involving the remaining high-energy basis functions, and it is a $2N_H \times 2N_H$ matrix with N_H the number of high-energy basis functions. Finally, V_c describes the coupling of the low- and high-energy subspace, and evidently involves matrix elements between low-energy and high-energy basis functions. The key approximation we now introduce is to retain a dependence on the $\mathbf{k}_0$ vector (in the bilayer Brillouin zone) at which the electronic structure is evaluated only in the low-energy block of the Hamiltonian. We fix the high energy and coupling blocks to the form they take when $\mathbf{k}_0 = \mathbf{K}_B$, the high-symmetry K vector of the bilayer Brillouin zone. This approximation is justified and, as we will see, it works very effectively, due to the large energy separation between the high-energy and low-energy blocks.

Let us consider projection operators onto the low-energy subspace, $P_0 = \mathrm{diag}(1,1,1,1,0,\ldots)$, and high-energy subspace, $P_1 = \mathrm{diag}(0,0,0,0,1,\ldots)$. A standard down-folding procedure then allows us to recast the eigenvalue equation $(E - H)|\Psi\rangle = 0$ in the low-energy subspace as

$$[E - H_L - V_c(E - H_H)^{-1}V_c^\dagger]|\Psi_L\rangle = 0 \tag{12}$$

with $|\Psi_L\rangle = P_0|\Psi\rangle$. This equation is exact, and the price to be paid for this is that it is no longer linear in E but instead involves the Green's function $G_H(E) = (E - H_H)^{-1}$. Rather than following the usual approach of linearizing Eq. (12) in E, we instead note that $G_H(E)$ may be expressed as $G_H(E) = (E - H_H^{(0)} - V_H)^{-1}$, where $H_H^{(0)}$ is the intralayer part of the high-energy block (and hence is diagonal in **k**-vector indices) and V_H represents the interlayer coupling part of the high-energy block. Introducing the bare high-energy Green's function $G_H^{(0)}(E) = (E - H_H^{(0)})^{-1}$, which is simply the high-energy Green's function with the interlayer interaction "switched off," we may write the latter object as a Dyson series,

$$G_H(E) = G_H^{(0)}(E) + G_H^{(0)}(E)V_H G_H^{(0)}(E) + \cdots, \tag{13}$$

and insertion of this into Eq. (12) yields

$$\left[E - H_L^{(0)} - V_c\left(G_H^{(0)}(E) + G_H^{(0)}(E)V_H G_H^{(0)}(E) + \cdots\right)V_c^\dagger\right] \times P_0|\Psi\rangle = 0. \tag{14}$$

This is now in a convenient form in which to implement a low-energy approximation by setting $G_H^{(0)}(E) \approx G_H^{(0)}(0) = -[H_H^{(0)}]^{-1}$, which then immediately yields an eigenvalue problem for the low-energy subspace,

$$\left[E - H_L^{(0)} + V_c\left(\left[H_H^{(0)}\right]^{-1} - \left[H_H^{(0)}\right]^{-1}V_H\left[H_H^{(0)}\right]^{-1} + \cdots\right)V_c^\dagger\right] \times P_0|\Psi\rangle = 0, \tag{15}$$

which is evidently expressed as a multiple scattering expansion (MSE) in terms of interlayer scattering matrices V_H and low-energy propagators $[H_H^{(0)}]^{-1}$, with the multiplication together of these $2N_H \times 2N_H$ dimension matrices generating all possible scattering paths between the N_H high-energy **k** vectors. Premultiplication by the $4 \times 2N_H$ dimension V_c, and postmultiplication by the $2N_H \times 4$ dimension $V_c^\dagger$, ensures that these paths begin and terminate at one of the low-energy **k** vectors.

For an actual calculation, we restrict the high-energy basis to the three degenerate lowest-energy states (the three high-energy **k** vectors are labeled "H" in Fig. 1) and include only the first nonzero order in the MSE. The layer off-diagonal block of the effective Hamiltonian is thus given by

$$S = \sum_{i_1 i_2} [V_c]_{\mathbf{K}i_1}\left[\left[H_H^{(0)}\right]^{-1}\right]_{i_1}[V_H]_{i_1 i_2}\left[\left[H_H^{(0)}\right]^{-1}\right]_{i_2}[V_c^\dagger]_{i_2\mathbf{RK}}, \tag{16}$$

where i_1 and i_2 label the **k** vectors involved in the scattering path, and all objects are now of dimension 2×2 (the pseudospin degree of freedom). Inspection of Fig. 1 reveals that there are three scattering paths that connect **K** and **RK** and pass through only one of the high-energy **k** vectors labeled "H." The $[V_c]_{\mathbf{K}i_1}$ and $[V_H]_{i_1 i_2}$ are scattering operators similar to those of Table I, but differing by the inclusion of umklapp vectors in the phases, which occur as the high-energy states that couple to **K** lie outside the first Brillouin zone, and so umklapp vectors are needed to backfold these states. The zero-energy propagator is identical for all three high-energy states and has

the form

$$H_h = \begin{pmatrix} d_h & e_h \\ e_h^* & d_h \end{pmatrix}, \tag{17}$$

which describes a general high-energy block. For the case of an initial AA stacking and a rotation of $\theta = 21.78$ corresponding to the $(p,q) = (1,3)$ commensuration with 28 atoms in the unit cell, we find for the effective Hamiltonian

$$H(\mathbf{k}) = \begin{pmatrix} 0 & \hbar v_F k e^{i\theta_{\mathbf{k}}} & w & 0 \\ \hbar v_F k e^{-i\theta_{\mathbf{k}}} & 0 & 0 & 0 \\ w & 0 & 0 & \hbar v_F k e^{-i(\theta_{\mathbf{k}}-\theta)} \\ 0 & 0 & \hbar v_F k e^{i(\theta_{\mathbf{k}}-\theta)} & 0 \end{pmatrix}, \tag{18}$$

where w is an effective coupling amplitude given by

$$w = \frac{3t_K^2 t_h}{\left(|e_h|^2 - d_h^2\right)^2} (\mathrm{Re}[e^{-i\pi/3} e_h] - d_h)^2, \tag{19}$$

in which t_h is the Fourier transform of the interlayer hopping evaluated at the high-energy $\mathbf{k}$ vector, and t_K is the interlayer hopping evaluated at the high-symmetry K point. In a similar way for the case of a 38.21° rotation [corresponding to a $(p,q) = (3,5)$ commensuration with again 28 atoms in the unit cell], we find

$$H(\mathbf{k}) = \begin{pmatrix} 0 & \hbar v_F k e^{i\theta_{\mathbf{k}}} & w & 0 \\ \hbar v_F k e^{-i\theta_{\mathbf{k}}} & 0 & 0 & w e^{i\pi/3} \\ w & 0 & 0 & \hbar v_F k e^{-i(\theta_{\mathbf{k}}-\theta)} \\ 0 & w e^{-i\pi/3} & \hbar v_F k e^{i(\theta_{\mathbf{k}}-\theta)} & 0 \end{pmatrix}. \tag{20}$$

Equations (18) and (20) are just the two "SE odd" and "SE even" low-energy Hamiltonians obtained by Mele [15] on general symmetry grounds for the large-angle twist bilayer, but with now all parameters fixed by the underlying electronic structure. The band structure near the K point that results from the effective Hamiltonians Eqs. (18) and (20) is presented in Fig. 2 as the light dashed line, along with the full line, which is the exact tight-binding result using the same two-center approximation used to derive t_K, t_h, d_h, and e_h. (Numerical details of our tight-binding method can be found in Sec. V.) As can be seen, the agreement is rather good, with only small deviations being seen between the continuum approximations given by Eqs. (18) and (20) and the full tight-binding calculations.

IV. LOW-ENERGY THEORY AT SMALL TWIST ANGLES

We now consider the case for which the rotation angle of the bilayer is small, $\theta < 15°$; this regime is characterized by the emergence of a geometric moiré pattern and significant disruption of the Dirac spectrum as $\theta \to 0$. As has been mentioned, this breaking of the fourfold degeneracy is significant only for two specific commensuration cells, i.e.,

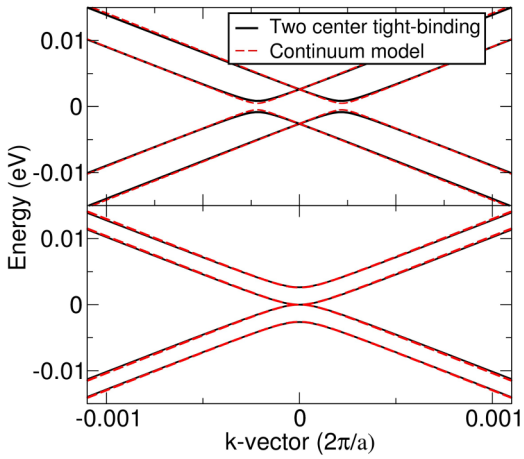

FIG. 2. Band structure of the two smallest commensurate twist bilayer structures: $\theta = 38.21°$ (top panel) and $\theta = 21.79°$ (bottom panel). For each of these twist angles, the supercell consists of 28 carbon atoms. The full dark (black) lines display the full two-center tight-binding approximation, and the light shaded (red) broken line displays that of the low-energy Hamiltonians Eq. (20) (top panel) and Eq. (18) (bottom panel).

those given by the rotation angles $\theta = 38.21°$ and 21.79°, and as numerous calculations attest it is negligible for other angles. In the small-angle limit, therefore, the existence of a second Dirac cone that folds back to $\mathbf{K}_B$ can be neglected as we have a twofold degeneracy of *all bands*. For this reason, we need to include only two Dirac cones in the theory, one from each layer. This simplifies the problem considerably, i.e., rather than the "four-cone" problem at large angles, we have a simpler "two-cone" problem. On the other hand, the problem is made more complicated (and the electronic structure made much richer) due to the fact that the momentum scale that governs the selection rule for Bloch states $g^{(c)}$ is vanishing in the small-angle limit. This entails the coupling together of a great many more states, whereas in the large-angle limit the electronic structure could be understood as a coupling (via multiple scattering expansions) of a relatively small number of states. For this reason, we require an approach that includes all scattering paths and, hence, all matrix elements of the interlayer interaction.

Given that the two Dirac cones that we are interested in are now separated by $\Delta K = |\mathbf{RK} - \mathbf{K}| = \frac{4}{3}\sin\frac{\theta}{2}$, which becomes small in the small-angle limit, and as we are only interested in a low-energy theory, we may consider a basis of Bloch functions that reside in some momentum sphere around $\mathbf{K}$ for layer-1 functions and around $\mathbf{RK}$ for layer-2 functions. In this case, all Bloch functions will have a momentum not too far from $\mathbf{K}$, and we may approximate the Fourier transform of the two-center hopping in Eq. (3) by $t(\mathbf{k}_1 + \tilde{\mathbf{G}}_{1i}) \approx t(K)$. The interlayer matrix elements given by Eq. (3) may now be written as

$$\left\langle \phi^{(1)}_{\alpha\mathbf{k}_1} \middle| H \middle| \phi^{(2)}_{\beta\mathbf{k}_2} \right\rangle = \frac{\Omega t_K}{(2\pi)^2} \sum_i [M_i]_{\alpha\beta} \delta_{\mathbf{g}_i^{(c)} = \mathbf{k}_2 - \mathbf{k}_1}, \tag{21}$$

where we have included in the matrix element explicitly the selection rule for single-layer Bloch states via the Kronecker δ function. With this approximation, we can construct a

continuum theory that reproduces all such matrix elements exactly as follows. We define the plane-wave spinor state from layer n as

$$\left|\phi^{(n)}_{\sigma_n \mathbf{k}_n}\right\rangle = \frac{1}{\sqrt{V}}|\sigma_n\rangle e^{i\mathbf{k}_n\cdot\mathbf{r}}, \tag{22}$$

where the pseudospinor $|\sigma_n\rangle$ is either pure pseudospin up, $|+\rangle = (1,0)$, or pure pseudospin down, $|-\rangle = (0,1)$, in the layer n portion of the 4-vector (with the other components of the 4-vector zero). Now consider the $\mathbf{r}$-dependent field

$$O(\mathbf{r}) = \frac{\Omega t_K}{(2\pi)^2}\sum_i M_i e^{-i\mathbf{g}^{(c)}_i\cdot\mathbf{r}}, \tag{23}$$

where the sum runs over the three coupling vectors of the selection rule derived in Sec. II. Matrix elements of the spinor plane-wave states from each layer with this field are

$$\int d\mathbf{r}\left\langle\phi^{(1)}_{\sigma_1\mathbf{k}_1}\right| O(\mathbf{r})\left|\phi^{(2)}_{\sigma_2\mathbf{k}_2}\right\rangle$$

$$= \frac{\Omega t_K}{(2\pi)^2}\sum_i \frac{1}{V}\int d\mathbf{r}\, e^{i(\mathbf{k}_2-\mathbf{k}_1-\mathbf{g}^{(c)}_i)\cdot\mathbf{r}}[M_i]_{\sigma_1\sigma_2} \tag{24}$$

$$= \frac{\Omega t_K}{(2\pi)^2}\sum_i [M_i]_{\sigma_1\sigma_2}\delta_{\mathbf{g}^{(c)}_i=\mathbf{k}_2-\mathbf{k}_1} \tag{25}$$

and thus reproduce exactly the tight-binding matrix elements in Eq. (21). If we define the diagonal 2×2 blocks of a 4×4 Hamiltonian to be the Dirac-Weyl operators of each layer, with the off-diagonal blocks given by $O(\mathbf{r})$ and its Hermitian conjugate, then we may write for the twist Hamiltonian

$$H = \begin{pmatrix} \hbar v_F\boldsymbol{\sigma}\cdot\mathbf{p} & O(\mathbf{r}) \\ O(\mathbf{r})^\dagger & \hbar v_F\boldsymbol{\sigma}\cdot\mathbf{R}^{-1}(\mathbf{p}-\Delta\mathbf{K}) \end{pmatrix}. \tag{26}$$

As the corresponding eigenvectors are now 4-vectors given by the direct product of layer space with pseudospin space, this Hamiltonian will reproduce both the layer off-diagonal matrix elements of tight-binding as well as layer diagonal elements (in the low-energy Dirac-Weyl approximation). Note that the shift $\Delta\mathbf{K}$ in the rotated layer Dirac-Weyl operator is required as we measure momentum in a global coordinate system centered on the unrotated cone.

In contrast to the large-angle case in which the interlayer interaction coupled together relatively few Bloch states from each layer and led to *constant* layer off-diagonal matrices, in the small-angle regime the interlayer coupling of many Bloch states drives the emergence of the real valued field $O(\mathbf{r})$. It should be remarked that Eq. (26) differs from the Hamiltonian derived in Ref. [8] only in the length scale $g^{(c)}$: the analysis in Sec. II yielded for this $g^{(c)} = \frac{4}{\sqrt{3}}\sin\frac{\theta}{2}$, whereas in derivation of Ref. [8] the coupling scale $\Delta K = \frac{4}{3}\sin\frac{\theta}{2}$ is found. As we shall demonstrate in subsequent sections, the use of the correct coupling scale brings the low-energy theory in the small-angle limit into complete agreement with full tight-binding calculations.

V. COMPUTATIONAL DETAILS

A. Tight-binding method

We use a simple $t(r) = A\exp(-Br^2)$ for the two-center hopping integrals with the constants A and B depending on whether the hopping is intra- or interlayer. For the former case, we use $A = 50$ eV, $B = 0.4373$ Å^{-2}, while for the latter we use $A = -8.4542$ eV, $B = 0.6649$ Å^{-2}. These parameters are obtained by minimizing via a simulated annealing method the error in eigenvalues (for selected $\mathbf{k}$ vectors) between the two-center tight-binding calculation of a number of few-layer graphene systems, and the corresponding systems calculated *ab initio* with the density-functional software package VASP [2,35–37]. We found it sufficient to use a database of single and Bernal stacked bilayer graphene along with the two smallest unit-cell twist bilayer commensurations with rotation angle $\theta = 21.79^\circ$ and 38.21°.

B. Two-center tight-binding calculations

We use the method described in Ref. [5] in which a basis of single-layer states is deployed to solve the tight-binding problem; we refer the reader to that manuscript for methodological details. It should be noted, however, that the correspondence of the selection rule for Bloch states derived in Sec. II can be found for single-layer states and leads to a simple Diophantine problem (Bezóut's identity) that results in an extremely efficient construction of the sparse interlayer blocks of the twist Hamiltonian. The use of a single-layer basis further dramatically increases computational efficiency, as to compute accurately the eigenvalues in some energy window ΔE requires only single-layer states in an energy window of $\approx 1.4\Delta E$. For a rotation angle of 0.74°, $(p,q) = (1,89)$ in the notation of Shallcross *et al.* [5,16], we find that to converge all eigenvalues in an energy range from -0.4 to $+0.4$ eV requires a Hamiltonian of dimension 360; the same problem using the standard localized orbital basis of the two-center tight-binding leads to a Hamiltonian of dimension 23 764. The resulting speedup of the former method compared to the latter is of the order of 10^5.

C. Low-energy calculations

In a similar way to the method outlined in Ref. [5], we solve the low-energy Hamiltonian using a basis of Dirac-Weyl states. That is, the basis consists of all eigenstates of both the unrotated (rotated) Dirac-Weyl operators that have momenta $\mathbf{k}$ that satisfy $|\mathbf{k}| < k_{\rm cut}$, with $k_{\rm cut}$ the radius of a momentum sphere centered at the Dirac point of the unrotated (rotated) cone. The vanishing of the momentum scale $g^{(c)}$ as $\theta\to 0$ obviously implies that for fixed $k_{\rm cut}$ the dimension of the resulting twist bilayer Hamiltonian in this basis will grow without bound. We find that the dimension is of the order of 10^2 to converge all eigenvalues in the energy window from -0.4 to $+0.4$ eV at a rotation angle of 0.90°, but it increases to 10^5 for 0.03°. Given that the matrix elements themselves can be obtained analytically from Eq. (26), the numerical bottleneck resides in diagonalizing the resulting Hamiltonian, and toward that end we use the SCALAPACK [38] subroutine PZHEEVR for the eigenvalue computations. To access the real-space wave functions, i.e., inverse Fourier transforming back to real space, standard fast Fourier transform (FFT) [39] is deployed.

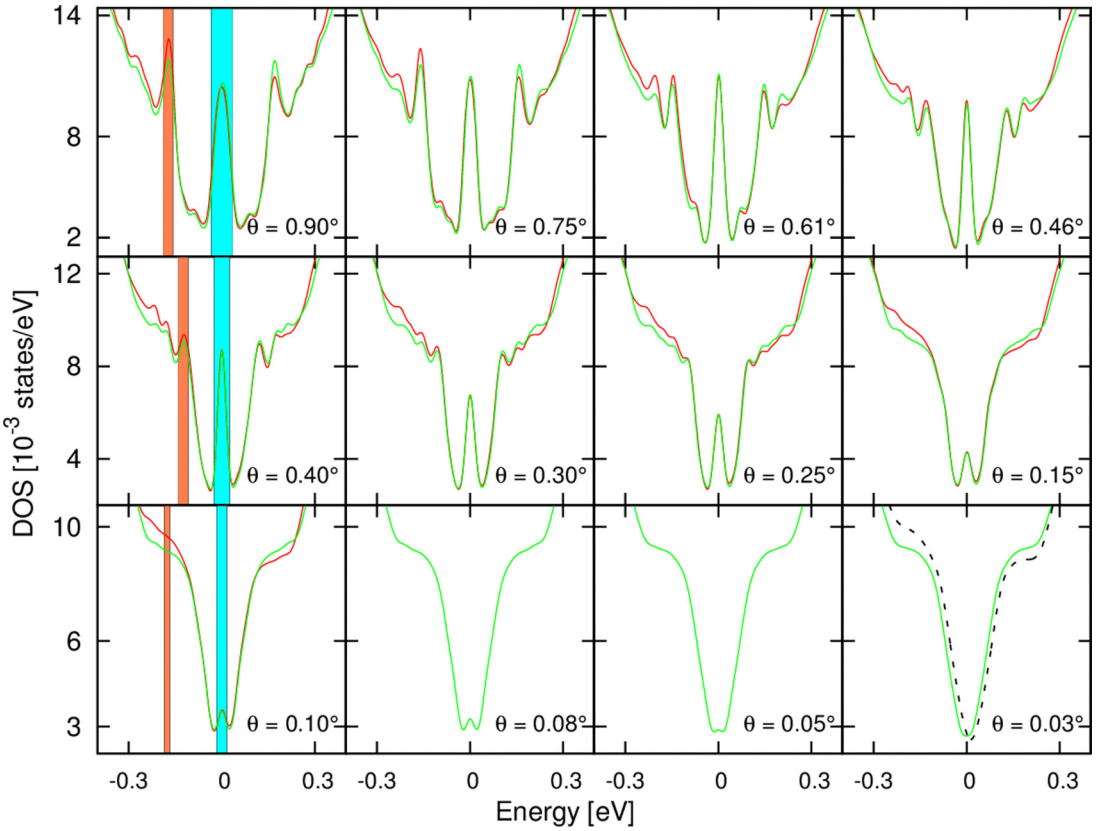

FIG. 3. *Density of states (DOS) in the small-angle limit*. Shown are calculations using the full two-center tight-binding scheme [dark shaded (red) full lines], along with the corresponding results generated using the low-energy Hamiltonian given by Eq. (26) [light shaded (green) full lines]. Shown are the DOS for twist angles from 0.90° to 0.03°; note that below 0.10° computational resources allowed only for calculation using the low-energy theory. For all cases shown, the DOS of both methods are seen to be in good agreement, particularly near the Dirac point at $E = 0$ eV. The light (cyan) shaded regions indicate the energy region of the central peak from which the electron density in the first column of Fig. 5 is constructed. Similarly, the dark shaded (red) regions illustrate the states summed over in the negative energy neighbor peak, from which the electron density displayed in the second column of Fig. 5 is constructed. The black dashed line in the $\theta = 0.03°$ panel is a superposition DOS constructed from the DOS of all possible interlayer stacking vectors, showing that at this angle the system has effectively electronically segmented into separate stacking regions.

VI. DENSITY OF STATES AND ELECTRON DENSITY

To test the veracity of the low-energy theory derived in Sec. IV, we first consider the density of states that results from Eq. (26), and, for a number of twist angles, we compare it to the DOS found using the full two-center tight-binding approach. This is shown in Fig. 3. One finds very good quantitative agreement between the low-energy and tight-binding calculations for all twist angles from 0.90° to 0.10° shown in Fig. 3. While near the Dirac point the agreement is nearly perfect, away from the Dirac point there are deviations that result from the fact that low-energy theory possesses, in the density of states, approximate electron-hole symmetry, and this is not the case for the tight-binding calculation. Note, however, that formal electron-hole symmetry does not exist for the Hamiltonian Eq. (26). In Ref. [5] it was observed that in the small-angle regime there appeared a region of approximate self-similarity in which a peak at the Dirac point persisted at the smallest angles. With the massively parallel implementation of both the single-layer basis tight-binding and the low-energy approaches, we can now push the DOS calculations to significantly smaller angles than have previously been achieved. Interestingly, we find that this regime of approximate self-similarity does not persist, and the Dirac point peak is continuously suppressed as θ decreases such that by $\theta = 0.03°$, the smallest angle that we were capable of calculating, it has entirely vanished.

This naturally invites the question, "what happens next?" To answer this question, we compare the $\theta = 0.03°$ DOS with a DOS that is the (normalized) sum of the DOS of all possible stacking arrangements of a graphene bilayer. Numerically, we consider a 20×20 mesh of interlayer shift vectors in the real-space unit cell of graphene, calculate the bilayer DOS for each shift vector, and then sum the 400 individual DOS results and normalize. The result of this procedure is shown as the black broken line in the $\theta = 0.03°$ panel of Fig. 3. The very close agreement between the "summed DOS of all stacking vectors" and the twist bilayer DOS suggests that by this angle the system has effectively electronically segmented into separate stacking regions, and no further significant changes in the DOS will occur for $\theta < 0.03°$. On the other hand, it should be stressed that this limit is somewhat academic. For a twist angle of 0.03°, the moiré length is already 4698 Å and it may well be that this is greater than some of the other length scales inevitably

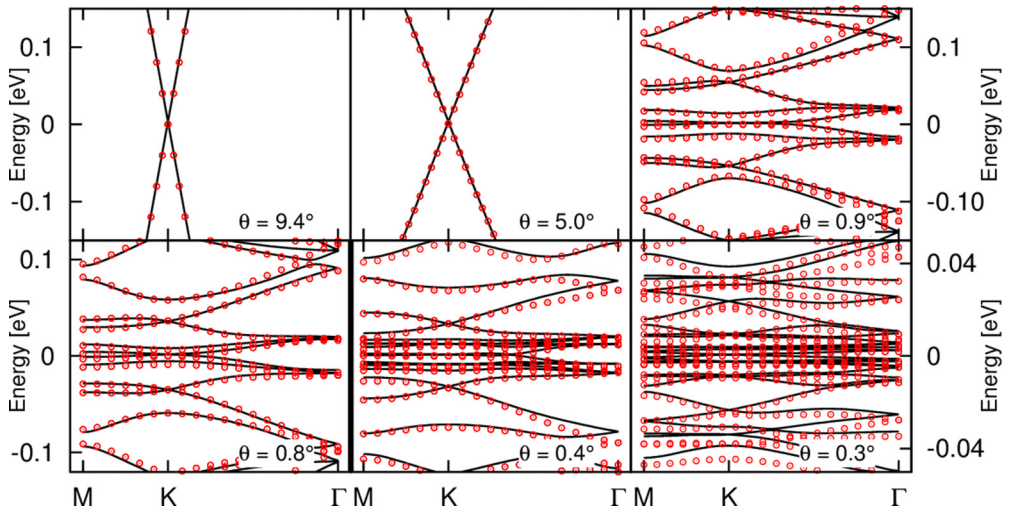

FIG. 4. Band structure of the twist bilayer plotted on a standard M-K-Γ path through the Brillouin zone. Open circles are tight-binding results, and full lines show the result provided by the low-energy effective Hamiltonian, Eq. (26). The pronounced set of flat "moiré bands" seen near the Dirac point correspond to the peak in the density of states of the bilayer spectrum shown in Fig. 3.

present: scattering of Bloch states due to the electron-electron interaction, or scattering introduced by disorder. Furthermore, there may arise structural changes of the moiré in the small-angle limit by the formation of domains separated by screw dislocations. Note, however, that it is not possible to calculate the limit for $\theta \to 0$ approaching from $\theta \neq 0$ exactly, as the unit-cell size diverges, and regions of AA and AB as well as all other possible shifts exist at each rotation angle. The case of Bernal stacking ($\theta = 0$) may be recovered from Eqs. (26) and (23) simply by setting $g^{(c)} = \frac{4}{\sqrt{3}} \sin \frac{\theta}{2}$ in the latter equation. The standard zeroth order in momentum approximation to the Bernal bilayer Hamiltonian is then immediately recovered, as may be verified from Eq. (23) and Table I:

$$H_{\text{Bernal}} = \begin{pmatrix} \hbar v_F \boldsymbol{\sigma}.\mathbf{p} & t_\perp \begin{pmatrix} 1 & 0 \\ 0 & 0 \end{pmatrix} \\ t_\perp \begin{pmatrix} 1 & 0 \\ 0 & 0 \end{pmatrix} & \hbar v_F \boldsymbol{\sigma}.\mathbf{p} \end{pmatrix} \tag{27}$$

(where the out-of-plane hopping constant is denoted by $t_\perp$).

A more detailed comparison between the low-energy theory and the tight-binding calculation is provided by the band structure of the twist bilayer, as shown in Fig. 4. The full symbols are the tight-binding results, with the continuous lines the band structure generated by the low-energy theory, and, as may be seen, for all angles a very good agreement is found. This agreement is particularly good for $\theta = 0.8^\circ$ and larger angles, although for the $\theta = 0.3^\circ$ case the agreement is somewhat worse (although this could not be seen in the Brillouin zone averaged density of states). One can note the appearance of a detailed set of almost dispersionless "moiré bands" in the small-angle limit; the band-structure counterpart of the density of states peak shown in Fig. 3. For all angles, we find an energy window within which a linear Dirac cone can be found, although already at $\theta = 0.4^\circ$ this window has reduced to 4 meV, below the precision of current experiments.

To further test the agreement between the low-energy approach and full tight-binding calculations, we now integrate the electron densities over the energy intervals highlighted in Fig. 3, that is, we consider the electron density determined by summing $|\Psi(\mathbf{r})|^2$ over all the states in the central peak (see the first column of Fig. 5), the satellite peak (the second column of Fig. 5), and an energy interval in the linear DOS region not shown in Fig. 3 (the third column of Fig. 5).

As may be seen, the electron densities integrated over the central peak show a strong localization on the AA spots of the moiré lattice. For a rotation angle of 0.90°, the localization effect is most strongly pronounced, while for 0.40° and 0.10° a weaker localization is seen, however even in these cases the density is of the order of 10 times greater in the AA regions than in the regions with the lowest electron density. This localization effect is well known and has been previously reported on a number of occasions; see Refs. [2,5,6]. Turning to a comparison of the low-energy approach with that of full tight binding, we see that the electron densities are in very good quantitative agreement between the two theories. It is noteworthy that even the fine structure of the density modulations away from the AA spot found in the 0.10° case are reproduced perfectly by the low-energy approach, demonstrating that this approach captures even details of the tight-binding calculations.

For electron densities obtained by integrating over the negative energy satellite peak, indicated by the dark shaded region in Fig. 3 and presented in the central column of Fig. 5, a similar situation may be observed. For a twist angle of 0.10°, the satellite peak has been suppressed into the prominent side regions around the Dirac point, and even though the DOS is not in perfect agreement at these energies, the intricate "star-shaped" high-density region on the AA spots is seen to be in remarkably good agreement between the tight-binding and low-energy Hamiltonian result. A curious exception to this very good agreement at low energies can be seen in the innermost "hexagon modulation" for the 0.40° case, which is rotated by 90° between the tight-binding and low-energy calculations. The reason for this curious discrepancy is not known.

Finally, we show in the third column of Fig. 5 the electron density in an energy region at which the DOS is linear and indistinguishable from that of single-layer graphene (we

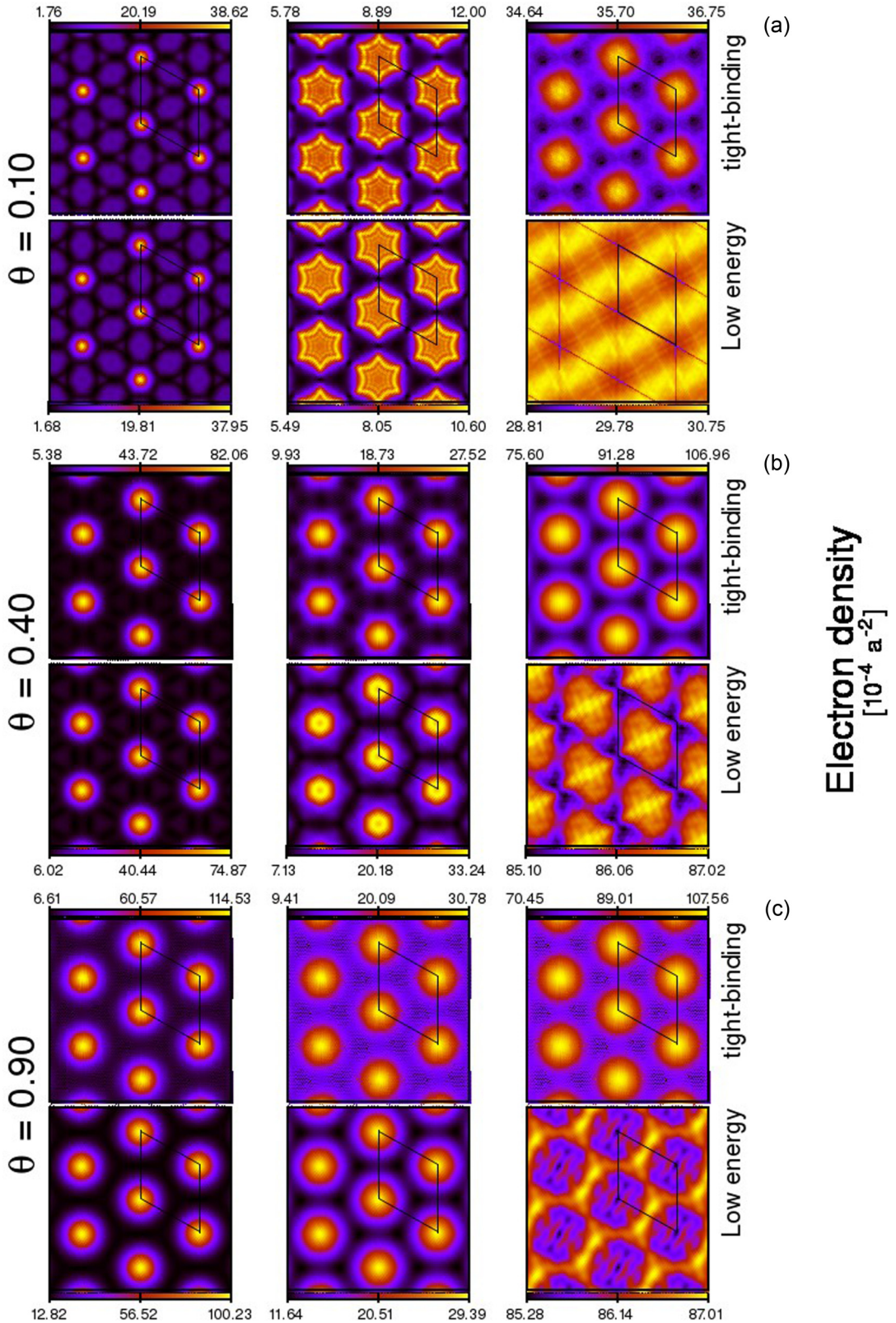

FIG. 5. Electron density formed by integrating $|\Psi(\mathbf{r})|^2$ over all states in the Dirac point peak indicated by the light shaded region in Fig. 3 (first column), the dark shaded region of the negative energy satellite peak (second column), and over all states in an energy window $-0.5 < E < -0.41$ eV for 0.90° and 0.40° and $-0.40 < E < -0.35$ eV for 0.10° (third column). Shown is the electron density at rotation angles of 0.90° (a), 0.40° (b), and 0.10° (c) obtained both from tight-binding calculations and the low-energy Hamiltonian of Eq. (26) as indicated.

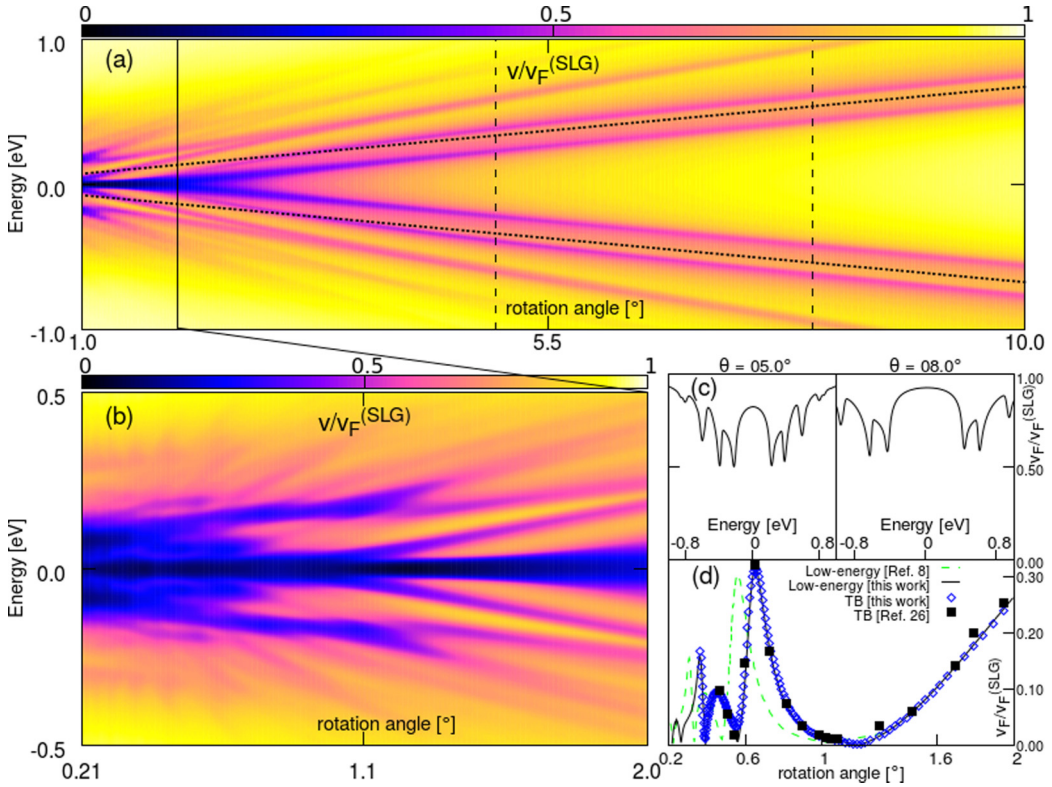

FIG. 6. Average band velocity as a function of twist angle of the bilayer and energy [panel (a)]. Valleys of reduced band velocity that arise from the interlayer coupling of the two Dirac cones may be seen, with such valleys directed toward the small-angle low-energy regime in which the average band velocity exhibits a complex (E,θ) dependence shown in panel (b). Panel (c) displays the average band velocity as a function of energy for two constant angles, and panel (d) shows the band velocity at the Dirac point (not averaged). In this panel, calculations using the low-energy Hamiltonian of this work [Eq. (26)] are shown as the solid black line, the low-energy Hamiltonian of Bistritzer *et al.* [8] is shown as the light dashed line, and full tight-binding calculations are shown both from this work (blue diamonds) and from Ref. [26] (black squares). The "magic angle" structure seen in panel (d) is to some extent washed out by convolving with a Gaussian, thus it is more difficult to detect in panel (b).

integrate states in an energy window $-0.50 < E < -0.41$ eV for 0.90° and 0.40° and $-0.40 < E < -0.35$ eV for 0.10°). In the tight-binding calculations, it is apparent that there is only a weak modulation of the density induced by the moiré, although this modulation again features the high-density region at the AA spots. This density modulation, however, is not well reproduced by the low-energy Hamiltonian, indicating that it is now operating outside its region of applicability. We can conclude, therefore, that the fine structure of the tight-binding calculation is not accessible by the low-energy approach outside an energy window of $\approx\pm 0.4$ eV about the Dirac point.

VII. BAND VELOCITIES AND FERMIOLOGY

Having established the excellent agreement between the low-energy Hamiltonian, Eq. (26), and full tight-binding calculations, we will now explore further the small-angle physics on the basis of the low-energy approach alone. Of crucial importance to the transport physics of the twist bilayer (and more generally the response properties of the bilayer) is the topology of the constant energy surfaces, and the averaged band velocity on these surfaces. The latter property is also, as we shall now demonstrate, very instructive for visualizing the complex electronic structure of the twist bilayer. The computational efficiency of the low-energy Hamiltonian, Eq. (26), allows for easy computation of constant energy surfaces and band velocities in the small-angle regime. We motivate the presentation of these results both by their intrinsic usefulness in understanding the twist bilayer, but also by the fact that (i) it is likely possible to shift the Fermi energy away from the Dirac point by doping without significantly changing the electronic structure of the bilayer, and (ii) the single-particle band structure at all energies is required for many-body calculations of the twist bilayer.

Panel (a) of Fig. 6 shows a density plot of the band velocities averaged by simply convolving each eigenvalue by a Gaussian of width 26 meV and determined for energies $-1 < E < 1$ eV and rotation angles $1^\circ < \theta < 10^\circ$. The appearance of a series of "valleys" of reduced average band velocity may be seen. These result from states from the Dirac cones from each layer that are connected by the coupling vectors $\mathbf{g}_i^{(c)}$, in particular the vector $\mathbf{g}_1^{(c)} = \mathbf{0}$, which corresponds to simple intersection points of the two cones. At such coupling points, bands from each layer hybridize, leading to the opening of a local gap in the cone structure and a reduction of the average band velocity in this energy region. The dashed lines seen in panel (a) indicate the lowest-energy intersection between the two cones, and, as may be seen, this corresponds very well with the most prominent band velocity valley. The band velocity valleys at higher energies correspond to intersections that occur

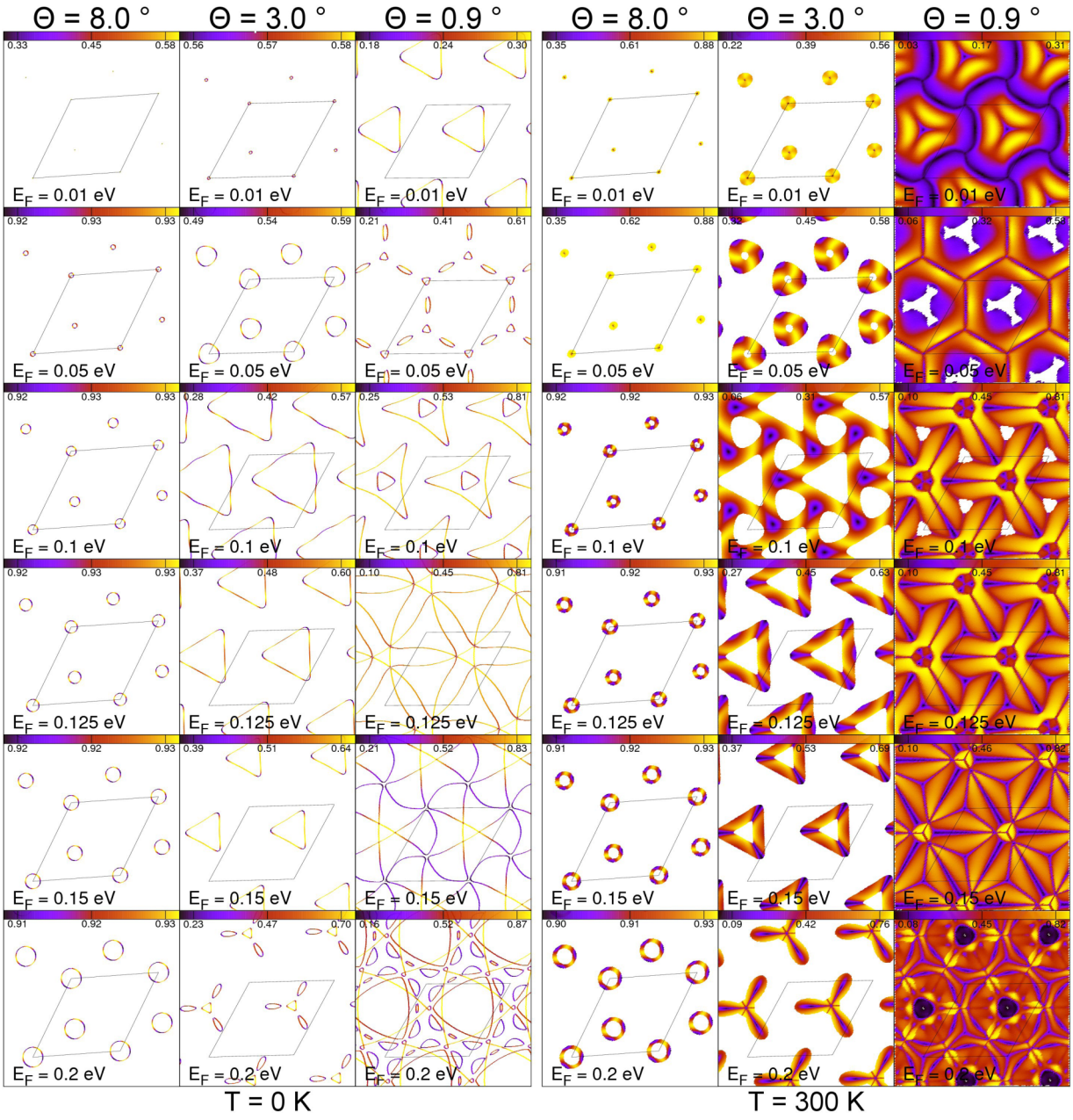

FIG. 7. Fermi surfaces at twist angles of $\theta = 8.0^\circ$, 3.0°, and 0.9° for a range of Fermi energies between 10 and 200 meV at both $T = 0$ (left panel) and $T = 300$ K (right panel). The color indicates the band velocity of the bands (presented as the ratio $v/v_F^{(\mathrm{SLG})}$) intersecting the constant energy surface. For the large twist angle of 8.0°, the fermiology is recognizably that of a Dirac cone; at smaller angles, the low-energy fermiology differs dramatically from the cone topology.

under "backfolding" by the vectors $\mathbf{g}_{2,3}^{(c)}$. Panel (c) displays the average band velocity as a function of energy for two representative angles indicated by the dashed vertical lines in panel (a). The reduction in band velocity corresponding to the valleys in the density plot can clearly be seen.

The band velocity valleys in panel (a) can all be seen to run toward the origin $E = 0$, $\theta = 0$. For angles at which a well-defined valley structure exists, it is legitimate to view the electronic spectrum as that of a Dirac cone manifold disrupted by interlayer hybridization at a discrete set of energies. However, in the region where these valleys converge toward the origin, the very concept of a Dirac cone becomes inapplicable. This can be seen in panel (b), in which an enlarged plot of this interesting region is presented. For angles $\theta < 0.5^\circ$, the average band velocity for energies $-0.25 < E < 0.25$ eV is $\approx 0.3 v_F^{(\mathrm{SLG})}$, and evidently the electronic structure has nothing to do with the Dirac cone of SLG or indeed any conical manifold. In panel (d) we plot the band velocity evaluated at the Dirac point, which is seen to exhibit the "magic angle" structure in which, for certain θ, the band velocity at the Dirac point approaches zero [8]. This structure is to a large extent washed out by convolving with Gaussians, and so it is not easy to see in panel (b). We should point out that while our results for the band velocity at the Dirac point

agree very well with the tight-binding calculations of Ref. [26] (despite a completely different scheme for the tight-binding parametrization), they are in disagreement with the results of the continuum model of Ref. [8]. This was noticed in Ref. [26], and it was shown that a simple rescaling would bring the results into perfect agreement. In the context of the low-energy model derived in this work, we recognize that this "rescaling problem" simply arises from the wrong choice of momentum scale: $\Delta K = \frac{4}{3}\sin\frac{\theta}{2}$ instead of $g^{(c)} = \frac{4}{\sqrt{3}}\sin\frac{\theta}{2}$. Despite the fact that we find "magic angles" in the lowest electron band, we note that their physical relevance is very limited, as other bands close to the Dirac energy do not show "magic angles," or the minima of their band velocities are at different angles. Consequently, the smoothing over many bands leads to the structure seen in panels (a) and (b) in Fig. 6.

The complex behavior in the strong-coupling small-angle low-energy limit implies significant disruption of the Dirac cone by the backfolding hybridization mechanism. To gain insight into the qualitative topological changes of the Dirac manifold, we now present constant energy surfaces in the low-energy regime. For all angles investigated, the $E = 0$ constant energy surface is found to be the same zero measure Fermi surface of single-layer graphene. This is a remarkable result, as for all $E \neq 0$ in the small-angle regime (as may be seen in Fig. 7), the topology of the constant energy surfaces differs dramatically from that of single-layer graphene. In Fig. 7 we show constant energy surfaces for energies $10 < E < 200$ meV, and for three representative angles, $\theta = 8^\circ, 3^\circ$, and 0.9°. The coloring of the constant energy surface indicates the magnitude of the band velocity $|v(\mathbf{k})|$ (scaled by the Fermi velocity of single-layer graphene).

The $\theta = 8^\circ$ data are presented for comparison with the two smaller angles that we subsequently discuss; at this angle and for energies less than 200 meV, the constant energy surfaces are rather simple, and they are exactly what would be expected from a Dirac cone, albeit with a somewhat reduced Fermi velocity as compared to single-layer graphene.

Turning to the case of a twist bilayer with $\theta = 3^\circ$ one notes that a strong trigonal warping of the cone sets in already at 100 meV; in single-layer graphene, such trigonal warping occurs only at very high energy. The magnitude of the band velocity on these constant energy surfaces can be seen to be much reduced from that of SLG, and while for the $\theta = 8^\circ$ bilayer $|v(\mathbf{k})|$ showed little variation over constant energy surfaces, at $\theta = 3^\circ$ significant variation is seen. This trigonally warped cone persists up to $\approx$200 meV, at which point the topology of the constant energy surface changes from a single sheet to multiple sheets.

Finally, for the case of $\theta = 0.9^\circ$ we see that this transition to a multiple sheet topology occurs almost immediately. Already at 10 meV we see the trigonal warping that occurred up to a

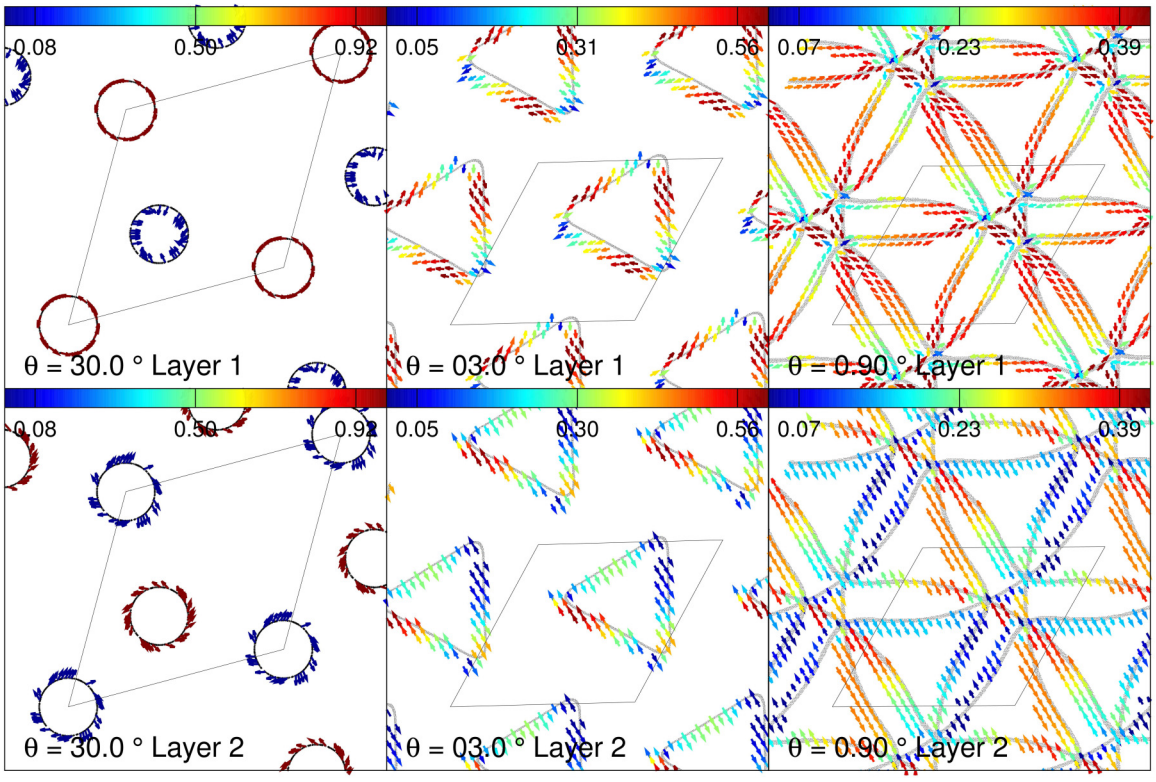

FIG. 8. Pseudospin texture of the twisted bilayer in the large- ($\theta = 30^\circ$), intermediate- ($\theta = 3^\circ$), and small- ($\theta = 0.9^\circ$) angle regimes. The Fermi energies of the Fermi surfaces are 0.9 eV for the large-angle case and 0.13 eV for the intermediate- and small-angle cases. The large-angle structure resembles the double vortex of a decoupled graphene bilayer, whereas in the intermediate-angle case a trigonally warped vortex is found. In the small-angle case, the pseudospin texture is seen to "flow" along the sixfold "arms" of the starlike Fermi surface. Note that the definitions of pseudospin up and pseudospin down differ between the two layers due to the rotation of the basis atoms of the second layer of the twist bilayer.

much higher energy of 150 meV for the 3° twist bilayer. Above 10 meV we see a multisheet and rapidly changing topology for all energies. The structure of these constant energy surfaces is remarkably rich, and even more baroque than the famous low-energy Fermi surface of graphite. Interestingly, while capturing the detail of the Fermi surface of graphite required very accurate *ab initio* methods, at these low energies the electronic structure is to a very high degree of accuracy described by the two-parameter Hamiltonian Eq. (26): the complexity of these constant energy surfaces is driven by *reciprocal space geometry of the Dirac cone backfolding*. One should also note again the significant variation of $|v(\mathbf{k})|$ over the constant energy surface, ranging from close to the SLG value to an order of magnitude less. As one would expect, regions with high $|v(\mathbf{k})|$ tend to be less susceptible to the dramatic changes in topology than regions with lower $|v(\mathbf{k})|$; compare, for instance, the constant energy surfaces at 125 and 150 meV. For a more complete visual representation of the energy dependence of the Fermi surfaces, we provide video clips as supplemental material [40].

Such rapid variations of the constant energy surface topology call into question the very usefulness of the concept of a Fermi surface in the small-angle regime. As an illustration of this, we show in the $T = 300$ K panels of Fig. 7 the plots in which the band velocity is averaged in an energy window $E - k_B T < E < E + k_B T$. For the case of an 8° twist, at which a Dirac cone is still well-defined, such a procedure leads to a "broadened" Dirac cone, but one still occupying a small portion of the Brillouin zone. However, for the case of a 0.9° rotation, the result is dramatic: there is now almost no part of the Brillouin zone in which for an interval of $2k_B T$ around an energy E there does not exist some single-particle eigenstate.

Furthermore, we analyze the dependence of the pseudospin on the rotation angle, as it has been recently reported that this quantity may explain measurable physical effects [41]. In Fig. 8 we present the pseudospin textures for three twist bilayers: in the large-angle ($\theta = 30°$), intermediate-angle ($\theta = 3°$), and small-angle ($\theta = 0.9°$) regimes. In the large-angle case, the pseudospin texture is that of single-layer graphene. In layer 1, a vortex of high-intensity pseudospin texture is seen on the Fermi circle situated at the K point, while in layer 2 we find a similar situation but with the high-intensity vortex situated now on the Fermi circle of the K^* point. Note that in the second layer, the pseudospin texture does not appear to be tangential to the Fermi surface; this simply results from the different definitions of pseudospin up and down in the two different layers, and it follows from the rotation of the basis vectors in layer 2.

In the intermediate-angle regime, a pronounced trigonally warped Fermi surface is found at 0.13 eV, and the pseudospin texture to some extent follows this warping to produce a "warped vortex" structure with, however, a highly pronounced modulation of the pseudospin texture now seen on the Fermi surface. Finally, in the small-angle regime this picture again holds with the pseudospin texture appearing to "flow" on the sheets of the richly structured Fermi surface: one notes that each "arm" of the sixfold starlike structure situated at the Γ point consists of a pseudospin vortex.

VIII. CONCLUSIONS

We have presented a unified theory of the graphene twist bilayer based on the notion of scattering paths that connect the K points of the two layers. In the large-angle limit, there are a small number of these scattering paths (three for the 28-atom commensuration cell) that may be conveniently expressed in real space as a multiple scattering series. In contrast, the small-angle limit presents an enormously increased number of scattering paths, which are conveniently encoded in the moiré field $S(\mathbf{r})$ that couples together the Dirac cones from each layer. In contrast to the small-angle limit, which involves only two Dirac cones, in the large-angle limit the scattering paths involve all four inequivalent Dirac cones of the twist bilayer. For large angles, we find this formalism leads to electronic versions of the symmetry-derived Hamiltonians of Mele [15], whereas in the small-angle limit we recover the Hamiltonian of Bistritzer and MacDonald [8], but with a different momentum coupling scale: instead of ΔK, the momentum transfer between the unrotated and rotated K points, a coupling momentum scale $g^{(c)}$ that in real space corresponds exactly to the moiré length D of the problem (ΔK leads to a real-space scale of $\sqrt{3}D$). We demonstrate that the small-angle effective Hamiltonian agrees almost perfectly with the low-energy electronic structure calculated by a tight-binding method, and thus that the rich electronic structure of the small-angle limit is essentially governed by just two parameters: the single-layer graphene Fermi velocity, $v_F^{(\mathrm{SLG})}$, and the Fourier transform of the interlayer hopping evaluated at the high-symmetry K point, $t(K)$. The baroque complexity of the small-angle limit—magic angles, band velocity valleys, electron localization patterns—is thus essentially geometric in origin and driven by the reciprocal space juxtaposition of mutually rotated single-layer Brillouin zones. At large angles, the effective Hamiltonians involve three additional electronic parameters connected to the high-energy states of the scattering paths, however once again we find that the agreement between the effective Hamiltonian and tight binding is nearly perfect.

By calculating the average band velocity systematically as a function of twist angle and energy, we are able to visualize a series of "band velocity valleys" that run toward a $\theta = 0$, $E = 0$ strong-coupling region. While for twist angles greater than $\approx 3°$ the electronic spectrum may legitimately be described as that of Dirac cones hybridized (by the interlayer interaction) at a discrete number of energies, in the small-angle region, in particular for $\theta < 0.5°$, we find that the Dirac cones are entirely destroyed by hybridization. In this small-angle regime, by deploying massively parallel calculations we are able to track the density of states (DOS) of the bilayer all the way to a twist angle of 0.03° at which the system electronically segments into distinct stacking regions, and thus no further change to the DOS will occur at smaller angles.

ACKNOWLEDGMENTS

This work was supported by the Collaborative Research Center SFB 953. One of us (S.S.) acknowledges the hospitality of I.I.T. Roorkee, India, during which an early version of the manuscript was worked on.

[1] L.-J. Yin, J.-B. Qiao, W.-X. Wang, Z.-D. Chu, K. F. Zhang, R.-F. Dou, C. L. Gao, J.-F. Jia, J.-C. Nie, and L. He, Tuning structures and electronic spectra of graphene layers with tilt grain boundaries, Phys. Rev. B **89**, 205410 (2014).

[2] W. Landgraf, S. Shallcross, K. Türschmann, D. Weckbecker, and O. Pankratov, Electronic structure of twisted graphene flakes, Phys. Rev. B **87**, 075433 (2013).

[3] A. Jorio and L. G. Cançado, Raman spectroscopy of twisted bilayer graphene, Solid State Commun. **175–176**, 3 (2013).

[4] X. Zou, J. Shang, J. Leaw, Z. Luo, L. Luo, C. La-o vorakiat, L. Cheng, S. A. Cheong, H. Su, J.-X. Zhu, Y. Liu, K. P. Loh, A. H. Castro Neto, T. Yu, and E. E. M. Chia, Terahertz Conductivity of Twisted Bilayer Graphene, Phys. Rev. Lett. **110**, 067401 (2013).

[5] S. Shallcross, S. Sharma, and O. Pankratov, Emergent momentum scale, localization, and van Hove singularities in the graphene twist bilayer, Phys. Rev. B **87**, 245403 (2013).

[6] P. San-Jose, J. González, and F. Guinea, Non-Abelian Gauge Potentials in Graphene Bilayers, Phys. Rev. Lett. **108**, 216802 (2012).

[7] E. J. Mele, Interlayer coupling in rotationally faulted multilayer graphenes, J. Phys. D **45**, 154004 (2012).

[8] R. Bistritzer and A. H. MacDonald, Moiré bands in twisted double-layer graphene, Proc. Natl. Acad. Sci. (USA) **108**, 12233 (2011).

[9] A. Luican, G. Li, A. Reina, J. Kong, R. R. Nair, K. S. Novoselov, A. K. Geim, and E. Y. Andrei, Single-Layer Behavior and its Breakdown in Twisted Graphene Layers, Phys. Rev. Lett. **106**, 126802 (2011).

[10] M. Kindermann and P. N. First, Phys. Rev. B **83**, 045425 (2011).

[11] G. Li, A. Luican, J. M. B. Lopes dos Santos, A. H. Castro Neto, A. Reina, J. Kong, and E. Y. Andrei, Observation of Van Hove singularities in twisted graphene layers, Nat. Phys. **6**, 109 (2010).

[12] G. Trambly de Laissardiére, D. Mayou, and L. Magaud, Nano Lett. **10**, 804 (2010).

[13] E. Suárez Morell, J. D. Correa, P. Vargas, M. Pacheco, and Z. Barticevic, Flat bands in slightly twisted bilayer graphene: Tight-binding calculations, Phys. Rev. B **82**, 121407 (2010).

[14] D. L. Miller, K. D. Kubista, G. M. Rutter, M. Ruan, W. A. de Heer, P. N. First, and J. A. Stroscio, Structural analysis of multilayer graphene via atomic moiré interferometry, Phys. Rev. B **81**, 125427 (2010).

[15] E. J. Mele, Commensuration and interlayer coherence in twisted bilayer graphene, Phys. Rev. B **81**, 161405 (2010).

[16] S. Shallcross, S. Sharma, E. Kandelaki, and O. A. Pankratov, Electronic structure of turbostratic graphene, Phys. Rev. B **81**, 165105 (2010).

[17] F. Varchon, P. Mallet, L. Magaud, and J.-Y. Veuillen, Rotational disorder in few-layer graphene films on 6H-SiC(000-1): A scanning tunneling microscopy study, Phys. Rev. B **77**, 165415 (2008).

[18] S. Shallcross, S. Sharma, and O. A. Pankratov, Quantum Interference at the Twist Boundary in Graphene, Phys. Rev. Lett. **101**, 056803 (2008).

[19] S. Shallcross, S. Sharma, and O. A. Pankratov, Twist boundary in graphene: Energetics and electric field effect, J. Phys. Condens. Matter **20**, 454224 (2008).

[20] J. Hass, F. Varchon, J. E. Millán-Otoya, M. Sprinkle, N. Sharma, W. A. de Heer, C. Berger, P. N. First, L. Magaud, and E. H. Conrad, Why Multilayer Graphene on 4H-SiC(0001) Behaves Like a Single Sheet of Graphene, Phys. Rev. Lett. **100**, 125504 (2008).

[21] J. M. Campanera, G. Savini, I. Suarez-Martinez, and M. I. Heggie, Density functional calculations on the intricacies of moiré patterns on graphite, Phys. Rev. B **75**, 235449 (2007).

[22] J. M. B. Lopes dos Santos, N. M. R. Peres, and A. H. Castro Neto, Graphene Bilayer With a Twist: Electronic Structure, Phys. Rev. Lett. **99**, 256802 (2007).

[23] H. Schmidt, J. C. Rode, D. Smirnov, and R. J. Haug, Superlattice structures in twisted bilayers of folded graphene, Nat. Commun. **5**, 5742 (2014).

[24] B. Roy and K. Yang, Bilayer graphene with parallel magnetic field and twisting: Phases and phase transitions in a highly tunable dirac system, Phys. Rev. B **88**, 241107 (2013).

[25] K. Uchida, S. Furuya, J.-I. Iwata, and A. Oshiyama, Atomic corrugation and electron localization due to moiré patterns in twisted bilayer graphenes, Phys. Rev. B **90**, 155451 (2014).

[26] G. Trambly de Laissardière, D. Mayou, and L. Magaud, Numerical studies of confined states in rotated bilayers of graphene, Phys. Rev. B **86**, 125413 (2012).

[27] C. J. Tabert and E. J. Nicol, Optical conductivity of twisted bilayer graphene, Phys. Rev. B **87**, 121402 (2013).

[28] J. M. B. Lopes dos Santos, N. M. R. Peres, and A. H. Castro Neto, Continuum model of the twisted graphene bilayer, Phys. Rev. B **86**, 155449 (2012).

[29] E. J. Mele, Band symmetries and singularities in twisted multilayer graphene, Phys. Rev. B **84**, 235439 (2011).

[30] D. Smith and L. von Smekal, Monte Carlo simulation of the tight-binding model of graphene with partially screened Coulomb interactions, Phys. Rev. B **89**, 195429 (2014).

[31] J. F. Dobson, T. Gould, and G. Vignale, How many-body effects modify the van der waals interaction between graphene sheets, Phys. Rev. X **4**, 021040 (2014).

[32] R. W. Havener, Y. Liang, L. Brown, L. Yang, and J. Park, Van Hove singularities and excitonic effects in the optical conductivity of twisted bilayer graphene, Nano Lett. **14**, 3353 (2014).

[33] J. González, Magnetic and Kohn-Luttinger instabilities near a Van Hove singularity: Monolayer versus twisted bilayer graphene, Phys. Rev. B **88**, 125434 (2013).

[34] E. Suárez Morell, M. Pacheco, L. Chico, and L. Brey, Electronic properties of twisted trilayer graphene, Phys. Rev. B **87**, 125414 (2013).

[35] G. Kresse and J. Hafner, Ab initio molecular dynamics for liquid metals, Phys. Rev. B **47**, 558 (1993).

[36] G. Kresse and J. Furthmüller, Efficiency of ab-initio total energy calculations for metals and semiconductors using a plane-wave basis set, Comput. Mater. Sci. **6**, 15 (1996).

[37] G. Kresse and J. Furthmüller, Efficient iterative schemes for *ab initio* total-energy calculations using a plane-wave basis set, Phys. Rev. B **54**, 11169 (1996).

[38] L. S. Blackford, J. Choi, A. Cleary, E. D'Azevedo, J. Demmel, I. Dhillon, J. Dongarra, S. Hammarling, G. Henry, A. Petitet, K. Stanley, D. Walker, and R. C. Whaley, *ScaLAPACK Users' Guide* (Society for Industrial and Applied Mathematics, Philadelphia, PA, 1997).

[39] M. Frigo and S. G. Johnson, The design and implementation of FFTW3, Proc. IEEE **93**, 216 (2005); Special issue on Program Generation, Optimization, and Platform Adaptation.

[40] See Supplemental Material at http://link.aps.org/supplemental/10.1103/PhysRevB.93.035452 for visualizations of the energy dependence of the Fermi surfaces at $\theta = 8.0^\circ$, 3.0°, 0.9°, and 0.75° as video clips.

[41] D. Song, V. Paltoglou, S. Liu, Y. Zhu, D. Gallardo, L. Tang, J. Xu, M. Ablowitz, N. K. Efremidis, and Z. Chen, Unveiling pseudospin and angular momentum in photonic graphene, Nat. Commun. **6**, 6272 (2015).